Tribology International 190 (2023) 109036

Contents lists available at ScienceDirect

Tribology International

journal homepage: www.elsevier.com/locate/triboint

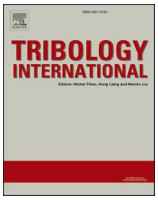

Turbulent lubrication model for journal-axial coupled hydrodynamic bearings without grooves

Guanying Xing, Song Xue, Jiacheng Han, Huaiyu Zuo, Run Hu, Zhengkai Tu, Xiaobing Luo *

School of Energy and Power Engineering, Huazhong University of Science and Technology, Wuhan 430074, China

ARTICLE INFO

Keywords:
Lubrication model
Journal-axial coupled bearing
Hydrodynamic levitation
Turbulent flow

ABSTRACT

A journal-axial coupled hydrodynamic bearing (JAHB) without groove was developed in our recent work. In JAHB, the fluid flow could produce the pressure difference to uplift the rotor. Nevertheless, the levitation mechanism of JAHB was not clarified, thus the quick design and optimization were blinded. This paper presents a turbulent lubrication model to predict the fluid pressure distribution in JAHB and the lubrication characteristics. The model takes full consideration of the coupled flow between the journal bearing and the axial bearing. The comparison between the experimental results and the calculations shows that the maximum error is below 15%. This work is expected to improve the fundamental understanding of the levitation phenomena in JAHB and their dependence on multiple design parameters.

1. Introduction

Bearings are utilized in various types of turbomachines and are essential for increasing the lifetime of such devices. However, for high-speed and heavy-loading scenarios, wear failure inherently exists in the mechanical bearings and adversely affects the operation stability [1–3]. Hydrodynamic levitation bearings [4,5], which can provide load capacities via the pressure difference in the process of fluid flow, have the advantages of low noise, high capacity and compactness. Considering the direction of the levitation force, they can be categorized into journal bearings [6–8] and axial bearings [9–11]. Fundamentally, the dynamic pressure effect [12,13] accounts for the generation of levitation forces in the journal bearing. When the rotor rotates eccentrically in a housing, the journal liquid film between them undergoes pressurization, resulting in a pressure difference. The axial bearing typically comprises a stationary disc and a coaxial rotating disc [4,7], on which the spiral microgrooves are curved. When the axial bearing is rotating, the fluid flow between the two discs is blocked and oriented by the slot-dam structure, and the pressure increases from the disc center to the disc periphery. Based on these principles, the capacity enhancement [14,15], stability promotion [3,16] and friction reduction [17] of groove-based levitation bearings were analyzed in tremendous studies to explore the introduction of different microgroove shapes and the corresponding structure optimizations. For instance, herringbone grooved journal bearings were demonstrated to cause less friction and improve the load carrying capacity [15,17,18]. In some remarkable works, scholars also attempted to integrate the grooved axial bearing and the journal bearing [8,10,19]. Such coupled levitation schemes can provide synthetic supporting capacities in multiple directions. The applications of coupled levitation bearings can be seen in centrifugal micropumps [1,19], rim driven thrusters [14,18] and so on [2]. However, for axial bearings, many studies have indicated that the load capacity is strongly correlated with the gap between the grooved rotating disc and stationary disc [10,18]. The results showed that the gap must be maintained within dozens of micrometers; otherwise, a dramatic reduction in levitation force was observed [11,19]. There was also a significant dependence of the load capacity decline on the disc deflection and microgroove blocking [9,20,21]. In engineering situations, however, the abovementioned high-precision assembly requirement, high-cost manufacturing and blocking problem of microgrooves severely restrict the widespread use of groove-based bearings [18].

It is clearly of vital importance to seek a simpler, lower cost and more reliable hydrodynamic levitation scheme. This motivates us to invent a novel journal-axial coupled hydrodynamic bearing (JAHB), as shown in our previous works [22,23]. JAHBs comprise a plain cylindrical rotor shrouded by a stationary eccentric-axis housing, as shown in Fig. 1(a). In such a case, it contains a journal bearing, that is, the journal liquid film between the rotor sidewall and the housing inner wall, and an axial bearing, that is, the axial liquid film between the rotor endwall and the housing endwall. In operation, the rotor can rotate at up to 20000

* Corresponding author.
E-mail address: luoxb@hust.edu.cn (X. Luo).

https://doi.org/10.1016/j.triboint.2023.109036
Received 8 August 2023; Received in revised form 15 September 2023; Accepted 22 October 2023
Available online 27 October 2023

revolutions per minute (RPM), and a radial levitation force (F_r) can be produced in the journal bearing according to the dynamic pressure effect [12]. Even though the physical mechanism of the axial levitation was not clear, our recent experimental study demonstrated that its ultimate load capacity reached many times over the rotor's weight [24]. The trajectory measurements demonstrated that the rotor of the JAHB levitated successfully under all rotating speeds [25]. Nevertheless, the lack of understanding of the levitation mechanism has severely restricted the quick design and optimization of JAHBs.

The analytical model of predicting the lubrication characteristics of JAHBs is obviously of much technological importance. In some studies, groove-based hydrodynamic bearings were modelled. For example, the pressure field in a textured journal bearing could be obtained with the Reynolds equation [13,16,26], which matched well with the experimental data [27]. Structural optimizations of groove-based bearings via analytical models were successfully conducted [6,28]. However, in previous research, there was hardly any analytical modeling of the plain axial bearing, which might be attributed to the unawareness of its capacity to provide a levitation force, as JAHBs did.

More importantly, given the continuous nature of the fluid flow in JAHBs, fluid transfer inherently exists between axial and journal liquid films. In such a case, the velocity profiles, viscous force behavior and therefore the pressure field in the whole bearing may be influenced by the fluid flow on the interface. Hence, the analytical model should be established subject to this coupling effect. However, in most theoretical studies, the fluid flows in journal bearings and axial bearings are considered two separate issues, and global optimization is limited [7,19,21,23]. Moreover, studies of fluid transfer in groove-based coupled bearings are available [28,29]. Because the peripheral region of the axial bearing was connected to the ends of the journal liquid film, the fluid in the journal bearing could exchange with the high-pressure fluid in the axial bearing, thus enhancing the overall pressure in the journal bearing [19]. In return, the pressure distribution in the journal bearing affected the interface flow rate and the velocity distribution in the axial bearing [29]. Specifically, the eccentricity of the rotor led to asymmetric interface fluid transfer and therefore caused asymmetric pressure distributions in the axial bearing [28]. The end leakage calculation of the journal bearing was developed [26] and enabled the quantification of the interface flow rate. Moreover, because of the larger pressure difference in the journal bearing at a higher rotating speed, the pressure unevenness in the axial bearing became more obvious [10]. Furthermore, the asymmetric pressure field in the axial bearing could generate a moment to the rotor, and an incline occurred [30]. The incline effect further changed the capacity characteristics of the hydrodynamic bearing [31]. A rotor dynamic study showed that the transient trajectory of the rotor was more consistent with the experiment compared with that in the uncoupled boundary condition [32]. Additionally, the hydrodynamic force results of coupled models also exhibited more satisfactory agreement with the experimental data [5,29]. We can see that such coupling phenomena in the fluid flow process cannot be neglected.

Regarding the analytical model considering the momentum transfer behavior, the interface boundary condition must be determined. From the current work [33], the interface pressure and flow rate might be resolved by the iterative approach, which regards mass conservation as the convergence criterion when calculating the whole bearing pressure field.

In this work, the flow equations are established considering the coupling effects between the journal bearing and the axial bearing in the turbulent regime, and their solutions with regards to the pressure distribution in JAHBs are derived. Furthermore, the experimental validation of the analytical model is discussed. The adoption of the analytical model is then presented to deepen the understanding of the levitation phenomena in JAHBs and their dependence on multiple design parameters. The coupling effects between the journal and axial bearings are analyzed. The lubrication performances of JAHBs are computed and evaluated, including the loading capacity and friction performance. These results may be helpful in designing effective hydrodynamic levitation bearings and developing various hydrodynamic devices based on this novel levitation principle.

2. Analytical model

Fig. 1(a) shows the schematic of a JAHB. The configuration of the JAHB is very simple and includes a plain hollow-cylinder rotor of radius r_1 shrouded by a stationary eccentric-axial housing of radius R and height H. In operation, the rotor rotates in the housing with an eccentricity of e and levitates, thus creating a journal liquid film with a cylindrical ring shape and a cylindrical-shaped axial liquid film. The axial clearance is s_2, and the inner radius of the rotor is r_0. Notably, the periphery of the axial bearing is combined with the end of the journal bearing, creating an interface for fluid exchange. In this section, the establishment of the analytical model for the fluid flow process in JAHBs is outlined. The structure parameters and operation conditions adopted in this study are presented in Table 1.

2.1. Analytical model for the fluid flow in a journal bearing

Fig. 2(a) schematically shows the top view of the fluid flow in the journal bearing. In this case, the thickness of the liquid film is much smaller than the height of the rotor. Thus, the following assumptions are obtained: (a) the pressure change along the film thickness direction is omitted, (b) the flow is treated as incompressible and isothermal and (c) Newtonian liquid is used. Since the rotating speed of the JAHB reaches over 10,000 RPM, according to the turbulence criterion [34], the flow condition actually lies in the turbulent regime. In such a case, the modified Reynolds equation, subject to the cavitation boundary condition and turbulence, governs the pressure distribution and can be obtained as [35]:

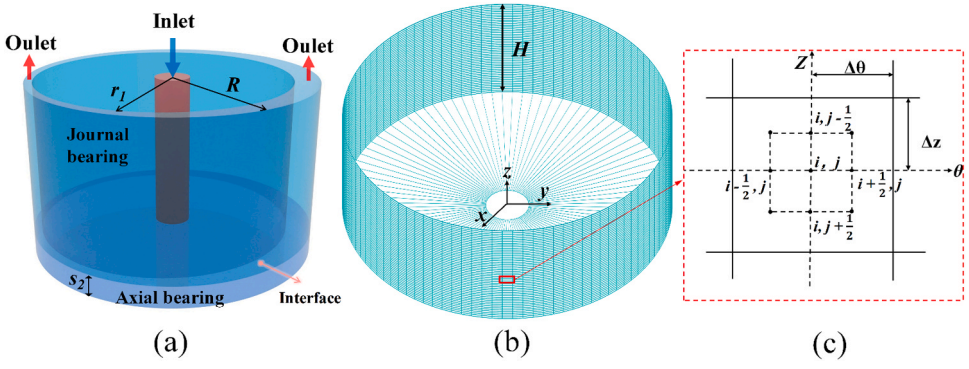

Fig. 1. (a) Schematic diagram of a JAHB. (b) Discretization of the computing domain. (c) Finite difference grids for the journal bearing model.

Table 1
JAHB structure and operating conditions.

Parameters		Symbol	Value
JAHB structure	Inner/Outer radius of the rotor	r_0/r_1	0.8/6.33 mm
	Rotor height	H	6 mm
	Inner radius of the housing	R	6.4 mm
	Eccentricity	e	0–0.8
	Axial clearance	s_2	0.5–3 mm
Experimental conditions	Ambient pressure	p_a	0
	Axial clearance	s_2	0.5–2 mm
	Inlet flow rate	Q_{inlet}	180–280 ml/min
	Eccentricity	e	0.5
	Rotating speed	ω	8000–12315 RPM
Calculation conditions	Discretization number	m/n	100/50
	Ambient pressure	p_a	30 KPa
	Axial clearance	s_2	1–3 mm
	Inlet flow rate	Q_{inlet}	15–50 ml/min
	Eccentricity	e	0.1–0.8
	Rotating speed	ω	8000–22000 RPM
	Inclination direction angle	φ'	0–180°
	Inclination extent	D_m	0–1
	Inclination angle	α	\
	Inclination eccentricity	e'	\
Lubricant properties	Type	\	Liquid-water
	Temperature	T_a	25 ℃
	Density	ρ	998.2 kg/m^3
	Cavitation pressure	p_c	3.17 KPa
	Dynamic viscosity	η	0.000899 pa·s

$$\frac{1}{r_1}\frac{\partial}{\partial\theta}\left(\frac{h^3}{\eta k_\theta}\frac{\partial p}{\partial\theta}\right)+\frac{\partial}{\partial z}\left(\frac{r_1 h^3}{\eta k_z}\frac{\partial p}{\partial z}\right)=6\omega r_1\frac{\partial(\Phi h)}{\partial\theta} \tag{1}$$

subject to

$$p = p_a \ at \ z = H \tag{2}$$

$$p = P_{interface} \ at \ z = 0 \tag{3}$$

$$\Phi = 1 \ at \ p \geq p_c \tag{4}$$

$$p = p_c \ \text{when} \ p < p_c \tag{5}$$

$$p = p_c \ \text{at} \ \Phi < 1 \tag{6}$$

$$\Phi = 1 \ \text{when} \ \Phi \geq 1 \tag{7}$$

where $p(\theta,z)$ and $\Phi(\theta,z)$ are the pressure distribution and liquid phase distribution over the rotor's cylindrical wall, respectively. Moreover, $\Phi(\theta,z)$ varies from 0 to 1. θ and z are the coordinate positions, and η and ω are the dynamic viscosity and rotational speed, respectively. p_c, p_a and $P_{interface}$ are the cavitation pressure, ambient pressure and pressure at the interface, respectively. k_θ and k_z are the turbulence coefficients, which can be obtained in the Ng-Pan model [36].

In practical operation, the unbalanced moment in the x/y direction may be exerted on the rotor; thus, inclination may occur. Fig. 2(c) shows a diagram of the inclined rotor. Here, o' is the center position of the rotor. o_1 and o_2 are the centers of the rotor upper end and bottom end, respectively. Fig. 3(d) is the top view of the rotor. c represents the clearance of the journal bearing and can be calculated as $R - r_1$. $c \times e'$ is the projection distance between o_1 and o_2. Moreover, e' is called the inclination eccentricity. φ' ($0 \leq \varphi' \leq \pi$) is the angle of the inclination direction. The film thickness $h(\theta,z)$ varies spatially because of the eccentricity and inclination and can be given by:

$$h(\theta,z) = c[1 + e\cos\theta] + ce'(z/H - 1/2)\cos(\theta - \varphi') \tag{8}$$

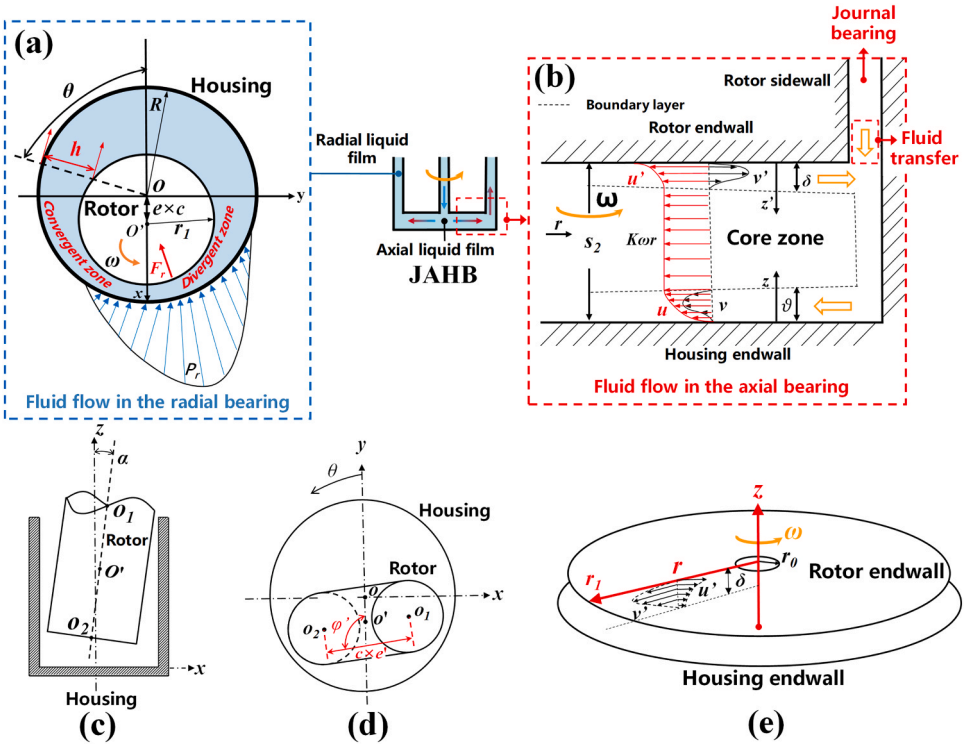

Fig. 2. (a) The top view of the JAHB and the fluid flow in the journal bearing. (b) The enlarged sectional drawing of the JAHB and the fluid flow in the axial bearing. (c) Diagram of the rotor incline. (d) The top view of the inclined rotor. (e) Profiles of the radial velocity v' and tangential velocity u' in the rotor boundary layer.

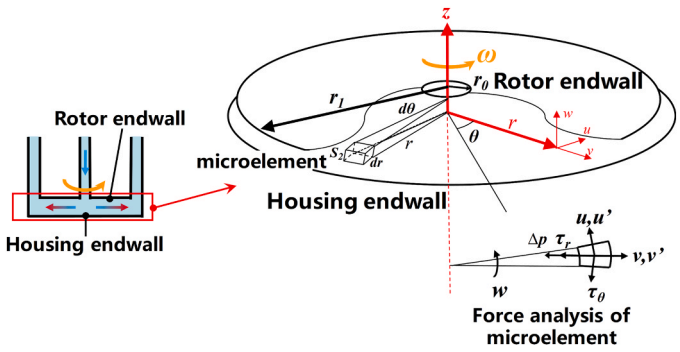

Fig. 3. Microelement division in the axial liquid film and the force analysis.

where H is the height of the rotor. To prevent contact between the rotor and the housing, there is an upper limit of the inclination. By conducting the geometric analysis in the rotor-housing system, $(c\times e')_{\max}$ can be calculated as follows:

$$(c\times e')_{\max} = 2c\left[\left(1-e^2\sin^2\varphi'\right)^{1/2} - e\left|\cos\varphi'\right|\right] \tag{9}$$

Here, we define D_m ($0 \le D_m < 1$) to describe the extent of the inclination. Thus,

$$ce' = (c\times e')_{\max}\times D_m \tag{10}$$

and the inclination angle α can be calculated as:

$$\alpha = \frac{c\times e'}{H} = \frac{(c\times e')_{\max}\times D_m}{H} \tag{11}$$

Finally, the position change brought by the inclination can be determined by φ' and D_m. For more details of the film thickness calculation with inclination, the reader can refer to Reference [30].

The solution of Eq. (1) can be obtained by using the finite difference method (FDM). In FDM, the computing domain is discretized into m nodes and n nodes in the θ and z directions, respectively, and the grid for computing is shown in Fig. 1(b) and (c). The key point is that all the partial derivative terms in Eq. (1) are replaced by the central differencing formulations. Furthermore, a successive overrelaxation (SOR) scheme is applied to solve $p(\theta,z)$ and $\Phi(\theta,z)$, and iterative calculations are conducted until the convergence criterion of 10^{-7} is met. Adequately fine discretization is conducted in FDM to ensure the mesh-independence of calculations. For further calculation details, the reader is referred to References [13,28].

After the pressure field is calculated, the radial levitation force (F_r) can be calculated by integrating the pressure along the cylindrical surface of the rotor:

$$F_r = \sqrt{F_x^{\,2} + F_y^{\,2}} \tag{12}$$

where

$$F_x = \int_0^{2\pi}\int_0^H p(\theta,z)\cos\theta dz r_1 d\theta \tag{13}$$

$$F_y = \int_0^{2\pi}\int_0^H p(\theta,z)\sin\theta dz r_1 d\theta \tag{14}$$

where F_x and F_y are the x component and y component of F_r, respectively. The friction torque of the journal bearing T_{f1} can be given by:

$$T_{f1} = \int_0^{2\pi}\int_0^H \left(\frac{h}{2}\frac{\partial p}{r_1\partial\theta} + \frac{\omega r\eta}{h}\right) r_1^{\,2} dz d\theta \tag{15}$$

Since the pressure gradient exists in the axial direction, the leakage flow rate of one calculation node on the interface can be calculated as [26]:

$$Q^i_{interface} = \left(\frac{h^3}{12k_z\eta}\frac{\partial p}{\partial z}\middle|z=0\right)\cdot r_1\Delta z\Delta\theta \tag{16}$$

The suffix i refers to the sequence number of the discretization in the θ direction.

2.2. Analytical model for the fluid flow in the axial bearing

The velocity profile in the axial bearing is shown in Fig. 2(b). As analyzed above, the rotor rotates at a super-high speed, and the flow pattern evolves into the turbulent regime. Based on the boundary theory, a thin flow occurs near the wall where the viscous forces dominate, and a large velocity gradient appears along the thickness direction. Regarding the JAHB, there are two boundary layers of thickness δ and ϑ, which flow near the rotor wall and the stationary wall, respectively. We will consider here the fluid flow over the rotor rotating with a sufficiently high angular velocity, due to which the effect of gravity on the momentum transfer is neglected and the pressure is constant in the axial direction. Additionally, the tangential velocity components are assumed to be u' and u in the boundary layers, as shown in Fig. 2(b). Furthermore, under the influence of the centrifugation effect, the fluid possesses radial velocity components of v' and v in the rotor and stationary boundary layers, respectively. Fig. 2(e) shows the spatial velocity distribution in the rotor boundary layer, where the velocity can be divided into the radial component v' and the tangential component u'. For simplification, the direction of the tangential velocity u/u' is drawn to be parallel to the radial velocity in red color in Fig. 2(b) and Fig. 4. And the tangential velocity V_θ/W_θ is drawn to be parallel to the axial velocity in red color in Fig. 4. Notably, between the two boundary layers, a "core zone" exists, wherein the radial velocity equals 0 and the tangential velocity remains constant, which is $K\omega r$, according to experimental studies [37,38] and our recent numerical simulation results [24]. Here, K is variable and may be related to the radial position of the boundary layer, and it is assumed to be a function of r.

The classic "one-seven" law [39] is applied to describe the profiles of the velocity distributions in the boundary layers. For the point $z' = 0$ located on the rotor surface, the radial component of the fluid velocity tends to that of the rotor wall, which is zero, and the tangential component of the fluid velocity equals ωr. Regarding the point $z' = \delta$ located on the boundary margin, the radial and tangential components are 0 and $K\omega r$, respectively. Thus, for the boundary layer near the rotor, the velocity distributions may be given by:

$$u' = r\omega\left\{1 - \left(\frac{z'}{\delta}\right)^{\frac{1}{7}} + K\left(\frac{z'}{\delta}\right)^{\frac{1}{7}}\right\} \tag{17}$$

$$v' = v_0^*\left(\frac{z'}{\delta}\right)^{\frac{1}{7}}\left(1-\frac{z'}{\delta}\right) \tag{18}$$

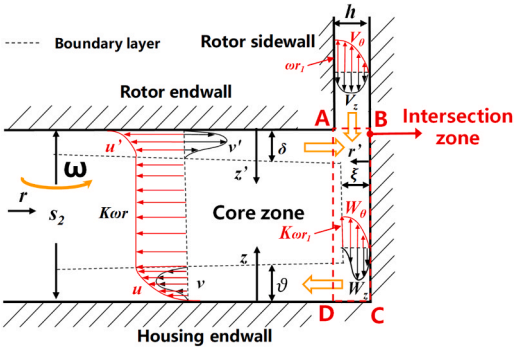

Fig. 4. The momentum transfer process in the intersection zone between the journal bearing and the axial bearing.

$$v_0^* = a*(1-K)r\omega \tag{19}$$

where r and z' are the radial and axial coordinates, respectively. v_0^* is the maximum value of the radial velocity, which can be assumed to be proportional to the tangential velocity difference between the core zone and the rotor nearby, that is, $a^*(1\text{-}K)\omega r$. Similarly, for the boundary layer near the housing endwall, we have

$$u = Kr\omega\left(\frac{z}{\vartheta}\right)^{\frac{1}{7}} \tag{20}$$

$$v = v_0\left(\frac{z}{\vartheta}\right)^{\frac{1}{7}}\left(1-\frac{z}{\vartheta}\right) \tag{21}$$

$$v_0 = -aK\omega r \tag{22}$$

In previous studies, the boundary flow pattern above a disc was examined [40,41], where the boundary layer thickness is proportional to $r^{3/5}$ and can be expressed as:

$$\delta = b(1-K)^2 r\Big/(Re)^{\frac{1}{5}} \tag{23}$$

$$\vartheta = fr\Big/(Re)^{\frac{1}{5}} \tag{24}$$

where f varies as a function of r and is determined by the continuity equation, which will be introduced later. b is a constant value for the boundary layer thickness calculation. Re is the local Reynolds number and is given by:

$$Re = \frac{\rho\omega r^2}{\eta} \tag{25}$$

For the Reynolds number covered in this paper, a, a^* and b are the boundary layer coefficients and are assumed to be 0.162, 0.162 and 0.526, respectively, according to similar experimental research on the velocity profiles in rotating-disc systems [37,38].

Considering the boundary flow between the rotor and the housing, the continuity relation indicates that the integration of the radial velocity components should equal the leakage flow rate from the journal bearing and can be derived as follows:

$$\int_0^{\vartheta} v\,dz + \int_0^{\delta} v'\,dz' = \frac{Q^i_{interface}}{\Delta\theta r_1} \tag{26}$$

Similar to the discretization conducted in the journal bearing, the calculation domain of the axial bearing is also divided into m parts in the θ direction, and i is the sequence number of the discretization, as shown in Fig. 1(c). By substituting Eqs. (18), (19) and (21)-(25), the resultant solution for Eq. (26) takes the following form:

$$f = \frac{1}{aK}\left(a^*b(1-K)^3 - \frac{120}{49}\frac{Q^i_{interface}}{\Delta\theta\omega {r_1}^3}Re^{\frac{1}{5}}\right) \tag{27}$$

Fig. 3 shows the selection of one microelement of thickness s_2 in the axial bearing, and the corresponding force analysis is conducted. In cylindrical polar coordinates, the radial momentum equation can be written as:

$$\frac{\partial}{\partial r}\left(r\int_0^{s_2} v^2 dz\right) - \int_0^{s_2} u^2 dz = -\frac{r}{\rho}\int_0^{s_2}\frac{\partial p}{\partial r}dz - \frac{r}{\rho}\tau_r\Big|_{z=0}^{z=S_2} \tag{28}$$

where τ_r is the radial shear stress on the wall surface. $p(r)$ is the pressure distribution on the rotor endwall. The left terms represent the radial momentum change brought by the velocity variation in the radial direction. The right first term indicates the effect of the pressure force, and the last term is the effect of the radial shear stress τ_r. The tangential momentum balance gives:

$$\frac{\partial}{\partial r}\left(r^2\int_0^{s_2} uv\,dz\right) = -\frac{r^2}{\rho}\tau_\theta\Big|_{z=0}^{z=S_2} \tag{29}$$

where τ_θ is the tangential shear stress on the wall surface, and the left term represents the angular momentum change of the microelement. To calculate the stress force from the wall, the Blasius empirical relations [37,39] are adopted. Hence, τ_θ and τ_r are determined from the following equations. On the rotor endwall, the following can be obtained:

$$\tau_{Rr} = 0.0225\rho\left(\frac{\eta}{\rho\delta}\right)^{\frac{1}{4}} v_0^*[(1-K)r\omega]^{\frac{3}{4}}\left\{\left(\frac{v_0^*}{(1-K)r\omega}\right)^2 + 1\right\}^{\frac{3}{8}} \tag{30}$$

$$\tau_{R\theta} = 0.0225\rho\left(\frac{\eta}{\rho\delta}\right)^{\frac{1}{4}}[(1-K)r\omega]^{\frac{7}{4}}\left\{\left(\frac{v_0^*}{(1-K)r\omega}\right)^2 + 1\right\}^{\frac{3}{8}} \tag{31}$$

On the housing endwall, the following can be obtained:

$$\tau_{sr} = -0.0225\rho\left(\frac{\eta}{\rho\vartheta}\right)^{\frac{1}{4}} v_0(Kr\omega)^{\frac{3}{4}}\left\{\left(\frac{v_0}{Kr\omega}\right)^2 + 1\right\}^{\frac{3}{8}} \tag{32}$$

$$\tau_{s\theta} = 0.0225\rho\left(\frac{\eta}{\rho\vartheta}\right)^{\frac{1}{4}}(Kr\omega)^{\frac{7}{4}}\left\{\left(\frac{v_0}{Kr\omega}\right)^2 + 1\right\}^{\frac{3}{8}} \tag{33}$$

Substituting Eqs. (17)–(24), (27) and (30–33) into Eqs. (28) and (29), followed by simplification, results in the ultimate non-linear differential equations:

$$\left\{\frac{5}{6}\frac{C_q}{R^{13/5}} - \frac{49}{240}a^*b(1-K)^2\right\}R\frac{dK}{dR} = 0.0225\left\{\frac{(a^{*2}+1)^{3/8}}{b^{\frac{1}{4}}}(1-K)^{\frac{5}{4}} - \frac{(a^2+1)^{\frac{3}{8}}}{f^{\frac{1}{4}}}K^{\frac{7}{4}}\right\} - \frac{5}{3}\frac{C_q}{R^{13/5}}K - 0.313a^*b(1-K)^3 \tag{34}$$

$$\frac{dP}{dP} = 2RK^2 + \frac{2R^{\frac{8}{5}}}{S\mathrm{Re}_{r_1}^{\frac{1}{5}}}\left\{F_1(R,K) - F_2(R,K)R\frac{dK}{dR}\right\} \tag{35}$$

where

$$F_1\left(R,K\right) = \frac{35}{69}\frac{C_q}{R^{13/5}}aK + \frac{b}{36}(1-K)^3\left(8K+1\right) - \frac{2}{9}K^2 f - 0.756a*b(1-K)^3\{aK + a*(1-K)\} - 0.0225\left\{\frac{a*(a*+1)^{3/8}}{b^{1/4}}(1-K)^{5/4} - a\left(a^2+1\right)^{3/8}\left(\frac{K^7}{f}\right)^{1/4}\right\} \tag{36}$$

$$F_2\left(R,K\right) = 0.207\left[-\frac{120}{49}a\frac{C_q}{R^{13/5}} + a*b(1-K)^2\{a - 4a* - 4K(a - a*)\}\right] \tag{37}$$

Here, Eqs. (34) and (35) govern the distributions of K and p over the radial direction, respectively. P, R and S are dimensionless coefficients, which can be given by $P = \frac{2p}{\rho w^2 r_1 z}$, $R = \frac{r}{r_1}$ and $S = \frac{s_2}{r_1}$, respectively. Moreover, C_q is the leakage coefficient from the journal bearing and can be defined as:

$$C_q = \frac{Q^i_{interface}}{\Delta\theta\omega r_1^3}(Re_{r_1})^{\frac{1}{5}} \tag{38}$$

It should be noted that the calculation domain is also circumferentially discretized into m sectors as shown in Fig. 1(b). There is a set of m× 2 nonlinear equations in the forms of Eqs. (34) and (35) to determine the spatial distributions of $K(r,\theta)$ and $p(r,\theta)$, respectively.

2.3. Model solution

In Sections 2.1 and 2.2, the analytical models of the fluid flows in the journal bearing and the axial bearing are established. However, the boundary conditions at the interface remain unknown, for instance, the boundary values of K and P at $r = r_1$ ($P_{interface}$) and the flow rate at the interface $Q^i_{interface}$. $P_{interface}$ and $Q^i_{interface}$ can be determined as follows. In the practical operation of JAHBs, the total inlet flow rate through the center hole of the rotor, Q_{inlet}, and the ambient pressure p_a are given. Initially, we set an initial value of $P_{interface}$ and substitute the boundary conditions of Eqs. (2)–(7) into Eq. (1) to resolve the pressure field in the journal bearing. Afterward, $Q^i_{interface}$ can be calculated by Eq. (16). According to mass conservation, the sum of $Q^i_{interface}$ along the interface should equal Q_{inlet}. Hence, iterative calculations are conducted by updating the values of $P_{interface}$ until the relative error between Q_{inlet} and $\sum_{i=1}^{m} Q^i_{interface}$ reaches the threshold, 10^{-7}. In this process, the Newton—Raphson method is applied to find $P_{interface}$. $P_{interface}$ in constant on the interface and the derivation can be seen in the Supplementary Materials.

When given the boundary values of K and P at $r = r_1$, Eqs. (34) and (35) can be solved by using the Runge—Kutta algorithm with MATLAB. From the results above, $P_{interface}$ can be assigned to P_{r1}. Here, to determine the boundary value of K at $r = r_1$, the tangential momentum balance is analyzed in the intersection zone ABCD. Fig. 4 shows the velocity profiles in Zone ABCD. Considering the momentum transfer process, the rotor boundary layer and journal bearing take angular momentum into ABCD through Edges AD and AB, respectively. The angular momentum leaves for the stationary boundary layer through Edge AD. In this process, when the fluid flows over the stationary walls (BC and CD), the friction works.

Thus, in ABCD, the sum of the angular momentum exit and ingress should equal that of the friction effect. Moreover, the momentum balance is described by:

$$\left[r_1{}^2\int_0^{\delta} u'v'dz'\right]_{r=r_0} = \frac{1}{\rho}\int_{r_1}^{r+h} r^2\tau_{S\theta}dr + \frac{(r1+h)^2}{\rho}\int_0^{S}\tau_{C\theta}dz + \left[r_1{}^2\int_0^{\theta} uvdz\right]_{r=r_0} + \int_{r_1}^{r_1+h} r^2V_zV_\theta dr \tag{39}$$

where V_z and V_θ are the axial and tangential components of the leakage flow into the journal bearing, respectively. From the "one-seven" law [39], we have:

$$V_\theta = \omega r_1\left(\frac{r'}{h}\right)^{\frac{1}{7}} \tag{40}$$

$$V_z = V_{\max}\cdot\left(1-\left|\frac{r'-0.5h}{0.5h}\right|\right)^{\frac{1}{7}} \tag{41}$$

$$V_{\max} = \frac{Q^i_{interface}}{0.82h\Delta\theta r_1} \tag{42}$$

ξ is the thickness of the boundary layer on the cylindrical wall, and $\tau_{C\theta}$ is the tangential shear stress, which is determined by the velocity distribution on the cylindrical wall. Similar to the assumptions adopted for the housing endwall, we have:

$$\tau_{C\theta} = \frac{0.0225\rho(a^2+1)^{\frac{3}{8}}r_1^2\omega^2}{(Re_{r_1})}\left(\frac{K_{r1}{}^7}{f_{r_1}}\right)^{\frac{1}{4}} \tag{43}$$

$$W_\theta = K_{r_1}\omega r_1\left(\frac{r'}{\xi}\right)^{\frac{1}{7}} \tag{44}$$

$$W_z = W_0\left(\frac{r'}{\xi}\right)^{\frac{1}{7}}\left(1-\frac{r'}{\xi}\right) \tag{45}$$

$$\xi = f_{r_1}r_1\Big/(Re_{r_1})^{\frac{1}{5}} \tag{46}$$

$$W_0 = [V_0]_{r_1} = aK_{r_1}\omega r_1 \tag{47}$$

where W_z and W_θ are the velocity components in the axial and tangential directions over the cylindrical wall, respectively. The derivation of the velocity profiles in ABCD can be found in the Supplementary Materials. The suffix r_1 represents the value obtained at $r = r_1$. By substituting Eqs. (40)-(47) into Eq. (36), the following expression of K_{r_1} is obtained:

$$\frac{49}{720}a*b(1-K_{r_1})^3+\frac{5}{6}C_qK_{r_1} = 0.0225(1+E)^2\left(S+E\right)(a^2+1)^{\frac{3}{8}}\left(\frac{K_{r_1}^3}{f_{r_1}}\right)^{\frac{1}{4}} - \int_{r_1}^{r_1+h} r^2V_zV_\theta dr\frac{\mathrm{Re}_{r_1}^{\frac{1}{5}}}{r_1^5\omega^2} \tag{48}$$

where $E = h/r_1$. Taking Eq. (48) into Eq. (34), the K distribution as a function of r can be calculated. By substituting K and P_{r1} into Eq. (35), the pressure distribution on the rotor endwall can be obtained. Fig. 5 shows the flow chart of the whole calculation process. Moreover, the axial levitation force (F_a) and the friction torque of the axial bearing T_{f2} can be given by:

$$F_a = \int_0^{2\pi}\int_{r_0}^{r_1} prdrd\theta \tag{49}$$

$$T_{f2} = \int_0^{2\pi}\int_{r_0}^{r_1} r^2\tau_{R\theta}drd\theta \tag{50}$$

The total friction torque of JAHB can be presented by:

$$T_f = T_{f1}+T_{f2} \tag{51}$$

3. Experimental validation

A levitation force measurement experiment was carried out to verify the analytical model proposed in Section 2. The general view of the test bench is shown in Fig. 6(a). The whole system comprises the water loop and the electromechanical parts. The water loop includes a water tank for fluid storage, a valve for flow rate control and a pump for fluid delivery. In the whole circulation, as Fig. 6(b) shows, the fluid enters from the inlet pipe and fills the clearance between the rotor and the housing, thus constituting a typical JAHB. The electromechanical components include a DC motor, a positioner, a force sensor and a precision displacement platform. In operation, the rotor is driven by the motor, as explained in the Supplementary Materials. The axial clearance s_2 can be adjusted by the precision displacement platform and the positioner. Before powering up, the rotor contacts the bottom of the housing. Then, the displacement platform is adjusted in the axial direction until the rotor also contacts the positioner. Afterward, the displacement platform is operated to slowly lift the positioner by the desired s_2. During operation, the rotor levitates and is limited by the positioner in the axial direction, maintaining the axial clearance at s_2. Thus, the axial clearance (s_2) can be precisely controlled.

The measurement principle is presented in Fig. 6(c). Notably, the sensor directly records the axial hydrodynamic force F_{static} acting on the housing. Then, the levitation force F_a can be derived from the axial momentum balance analysis. The resultant expression for the axial levitation force F_a takes the following form:

$$\rho Q_{inlet}(v_{out}-v_{in}) = F_{static}-F_a-\rho V_{clearance}g \tag{52}$$

where the term $\rho V_{clearance}g$ is the gravity of the fluid in the clearance between the rotor and housing. Q_{inlet} is given and represents the flow

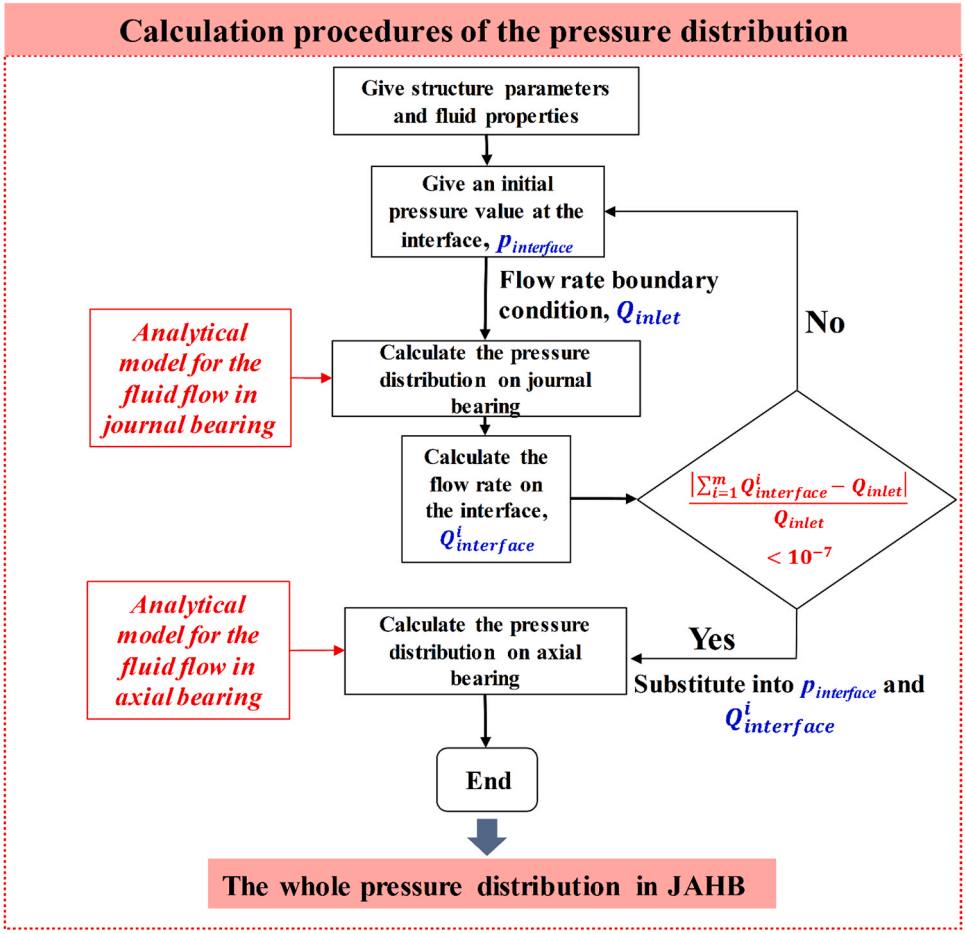

Fig. 5. Flow chart of the whole calculation process for the pressure distribution in JAHBs.

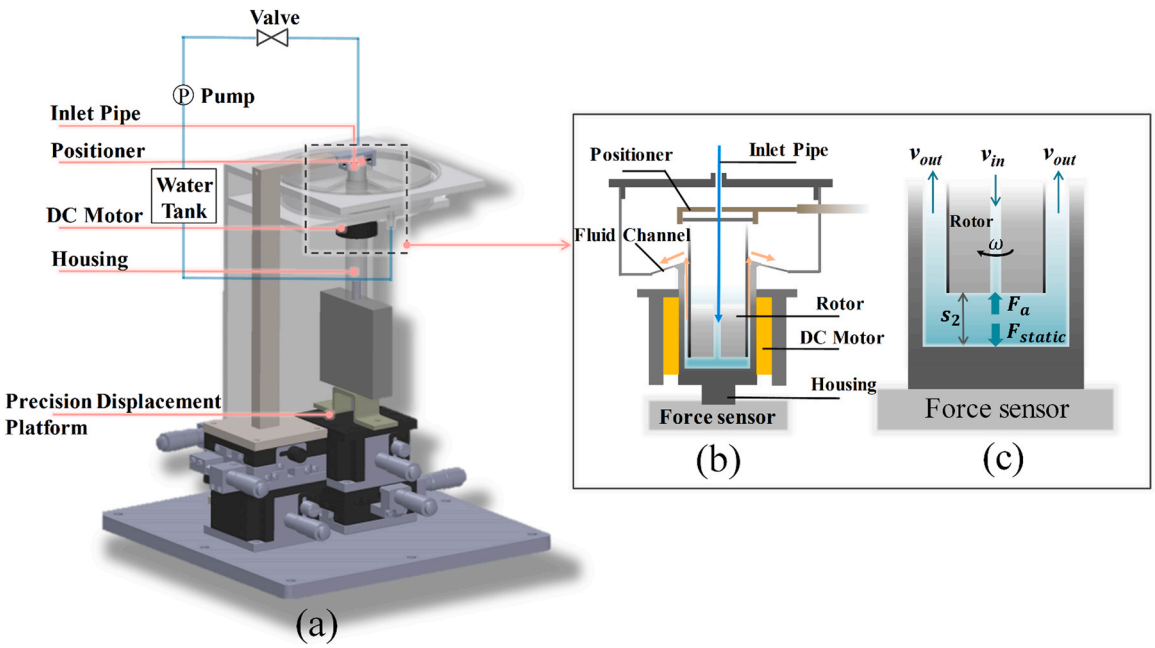

Fig. 6. (a) Schematic of the test bench for levitation force. (b) The sectional view of the test bench. (c) The measurement principle based on the momentum analysis.

rate. v_{in} and v_{out} represent the fluid velocities through the inlet and outlet, respectively. When the structure parameters of the test bench are known, $V_{clearance}$, v_{in} and v_{out} can be determined. The operating conditions are summarized in Table 1. For more details, the readers can refer to our published experimental work [24].

Fig. 7(d) shows a picture of the test facility. Measurements were

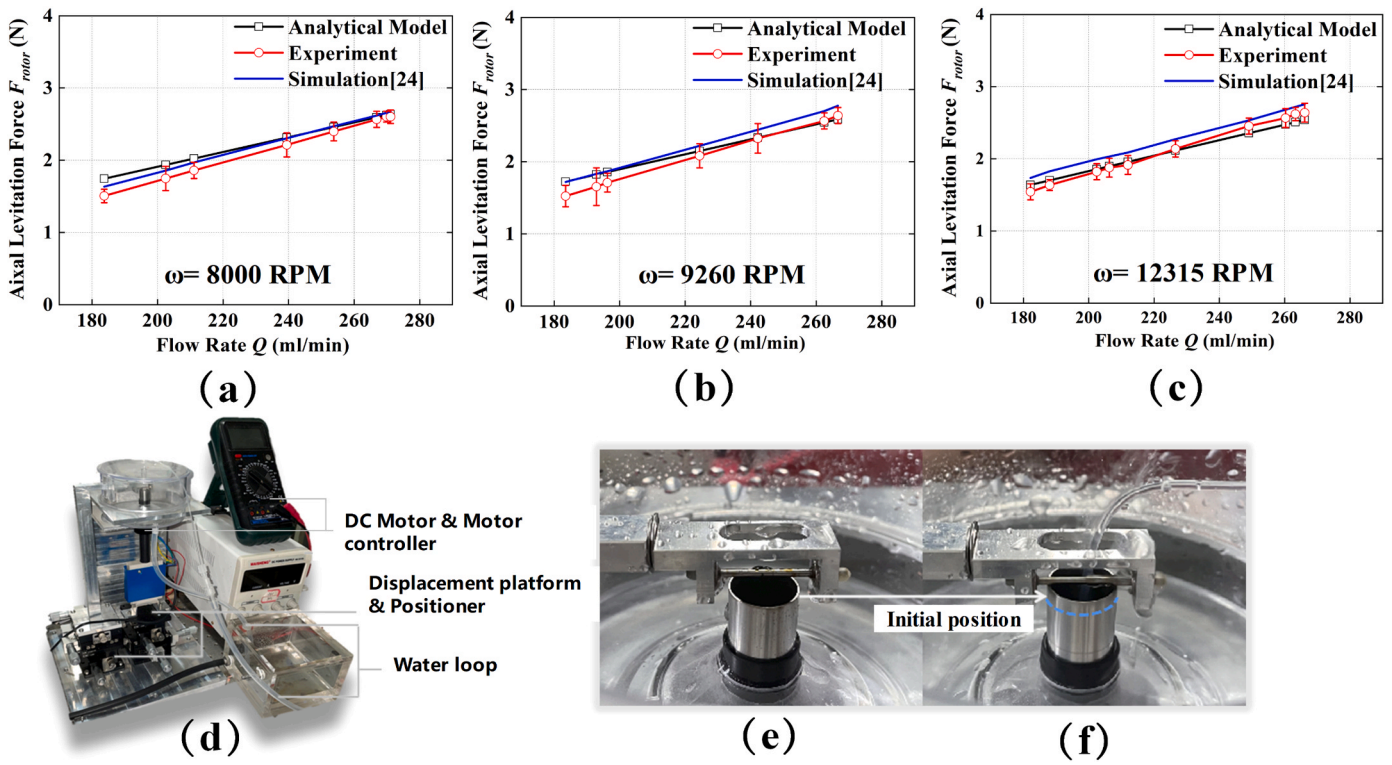

Fig. 7. Experimental, simulation [24] and calculation results of the axial levitation force of the JAHB at different rotating speeds. (a) 8000 RPM, (b) 9260 RPM and (c) 12315 RPM. (d) Picture of the test bench. (e) The initial position and (f) the operation position of the rotor.

conducted at different rotating speeds and flow rates, and each case was repeated three times to reduce random errors. The analytical model proposed in Section 2 is utilized to predict the axial levitation force under the experimental conditions. Fig. 7(a)-(c) present the calculated, simulated [24] and experimental levitation forces as functions of the flow rate for different rotating speeds. The experimental force variation and the corresponding standard deviation are also plotted. Satisfactory agreement between the experimental results and the predicted results is observed, which validates the analytical model. Specifically, at rotating speeds of 8000 RPM, 9260 RPM and 12315 RPM, the maximum errors between the measurement and the model are below 15%, 13% and 6%, respectively. Moreover, the error tends to decrease when increasing the rotating speed. Compared with the simulation results [24], the maximum calculation errors are less than 6.3%, 7.33% and 7.04% for 8000 RPM, 9260 RPM and 12315 RPM, respectively. However, for the same case, the CPU time required for the model is approximately 25 s in MATLAB, rather than 2.6 h for the numerical simulation. Thus, the analytical model is quite efficient and the code is easy to be coupled with the optimization algorithm, thus enabling the quick design of JAHB. For all the working conditions covered in the experiments, the axial levitation force increases almost linearly with the flow rate. Moreover, the levitation phenomenon is observed, as shown in Fig. 7(e) and (f). We can see that compared with the initial state, the rotor is uplifted by the axial levitation force in the operation state.

4. Results and discussion

On the basis of the analytical model, the dependence of the bearing characteristics, such as the load capacity and the friction torque, on multiple design parameters are analyzed in this section. Moreover, mechanistic insights into the close coupling between the journal bearing and the axial bearing, and therefore the influences on the lubrication performance, are presented in this section. Furthermore, the parameter settings are summarized in Table 1.

4.1. Investigation of the coupling effects

Fig. 8(a)-(c) present the overall view of the pressure field in JAHBs for different eccentricities at $\omega = 20000$ RPM and $Q_{inlet}= 40$ ml/min in non-inclined conditions. Due to the eccentric rotation of the rotor, the pressure gradients in the journal liquid film are circumferentially varying in nature, and pressure spikes and pressure valleys occur. It can be seen that the pressure rises radially on the rotor endwall as expected, thus confirming the levitation phenomenon. However, due to the uneven pressure distribution in the journal liquid film, the variation in the flow rate on the film interface is a function of the circumferential angle θ, causing the pressure field of the axial bearing to be inhomogeneous in the circumferential direction, as displayed in Fig. 8(a)-(c). Moreover, Fig. 8(d)-(f) show the interface flow rate ($Q^j_{interface}$ variation with θ at different eccentricities (e) and rotating speeds (ω). The results show that the non-uniform distribution of $Q^i_{interface}$ is more obvious with increasing eccentricity and ω. Furthermore, the profiles of u', v', u and v in the axial bearing, which are described by Eqs. (17), (18), (20) and (21), are displayed in Fig. 9(a) when $\theta = 0$. Here, the housing endwall is located at $z = 0$, and the rotor endwall is located at $z = 1$ mm. The insert diagram shows the top view of the JAHB and the selection of the circumferential angle θ. From Fig. 9(a), there exists a "core zone" in the axial bearing, where the tangential velocity remains constant and the radial velocity is zero. From the pressure distribution on the rotor endwall in Fig. 9(b), the fluid pressure increases along the radial direction due to the centrifugation force, while the pressure is asymmetric in the tangential direction caused by the circumferential-varying interface flow, as shown in Fig. 8 (d)-(f). Furthermore, to evaluate the effects of circumferential-varying interface flow on the pressure field, the radial pressure distributions on the rotor endwall at $Q^i_{interface} = -4.9 \times 10^{-6}$, -2.5×10^{-6}, 0, 2.5×10^{-6} and 4.9×10^{-6} m^3/s are presented in Fig. 10(a). We can see that with the increase in $Q^i_{interface}$, the pressure curve rises. The mechanism of this change is presented below.

A negative $Q^i_{interface}$ indicates that the fluid flows into the axial bearing, and this inward flow acts as an accelerated flow. When the

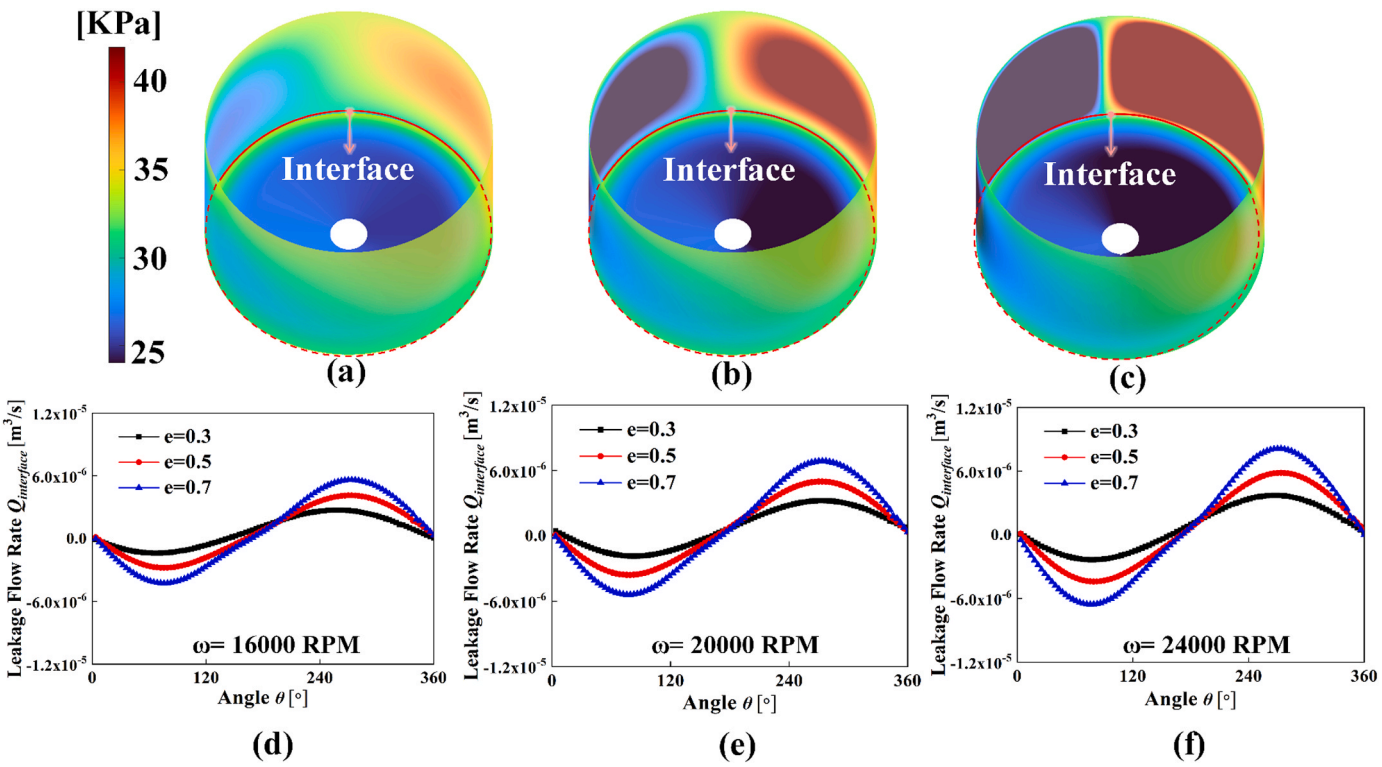

Fig. 8. Pressure distribution in the JAHB by the analytical model at Q_{inlet} = 40 ml/min, ω = 20000 RPM, s_2= 1 mm and different eccentricities (a) e= 0.3 (b) e= 0.5 and (c) e= 0.7. The interface flow rate variation curves with θ under different eccentricities at (d) ω = 16,000 RPM, (e) ω = 20000 RPM and (f) ω = 24,000 RPM.

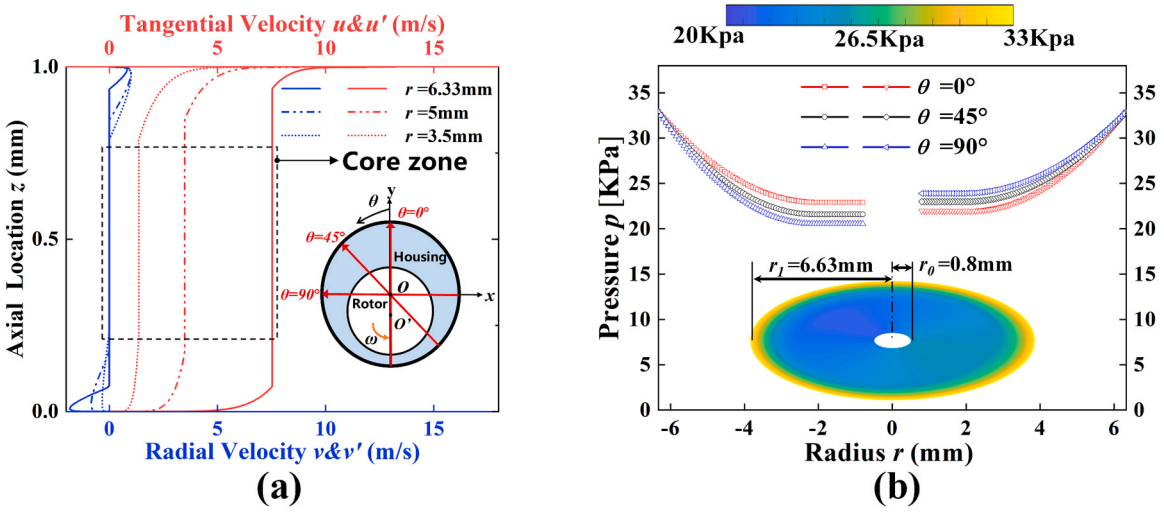

Fig. 9. (a) Velocity distribution in the axial bearing in the z direction at θ = 0 and (b) the pressure distribution in the axial bearing at different θ when e= 0.5, Q_{inlet} = 40 ml/min, ω = 20000 RPM and s_2= 1 mm.

inward flow takes angular momentum into the axial liquid film, a significant increase in the tangential velocity occurs in the core zone, which means a larger K. Moreover, the tangential velocity difference between the rotor and the fluid will decrease, resulting in a thinner boundary layer on the rotor, as shown in Eq. (23). Fig. 10(b) displays the plots of the boundary layer thickness and K as a function of the radius for different $Q^i_{interface}$ at $r = r_1$, 0.9 r_1 and 0.8 r_1. The results show that δ increases with $Q^i_{interface}$, while K decreases with $Q^i_{interface}$, manifesting the acceleration effect of the inward flow. Considering the form of Eq. (28), the term appearing with $\int_0^{S_2} u^2 dz$ becomes larger when K increases, causing a higher gradient of p and a more significant pressure reduction toward the disc center. The boundary theory illustrates that the velocity gradient mainly appears in the thickness direction. Then, the influence of the first term in Eq. (28) can be neglected. On the other hand, since the inward flow enters the stationary boundary layer, as shown in Fig. 2 (b), the radial velocity increases, causing a larger τ_{Sr}. However, τ_{Rr} decreases because of the smaller v_0* at higher K, according to Eqs. (19) and (30). Hence, the shear stress term in Eq. (28) decreases, also resulting in higher dp/dr. Moreover, from Fig. 10(a), when $Q^i_{interface}$ changes from 0 to $-$ 4.9 $\times$ 10^{-6} m^3/s, the minimum value of the pressure decreases from 24.84 KPa to 22.83 KPa. However, when $Q^i_{interface}$ increases from 0 to 4.9 $\times$ 10^{-6} m^3/s, the minimum value of the pressure only increases from 24.84 KPa to 26.25 KPa. It can be concluded that the influence of $Q^i_{interface}$ on the pressure field becomes weaker with increasing $Q^i_{interface}$.

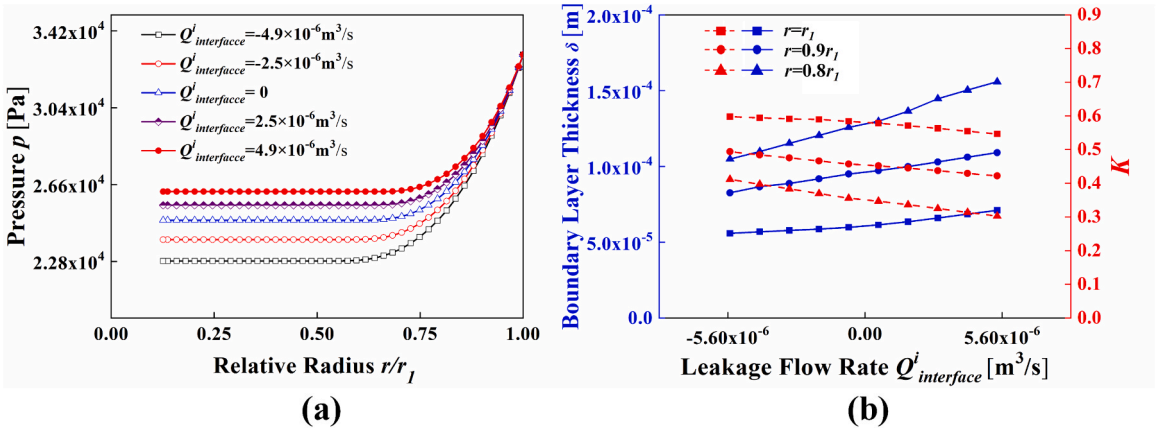

Fig. 10. (a) Pressure variation curves with the radius in the axial bearing under different $Q^i_{interface}$ values at ω = 20000 RPM and s_2= 1 mm. (b) Boundary layer thickness (δ) and K distributions with $Q^i_{interface}$ at different radii.

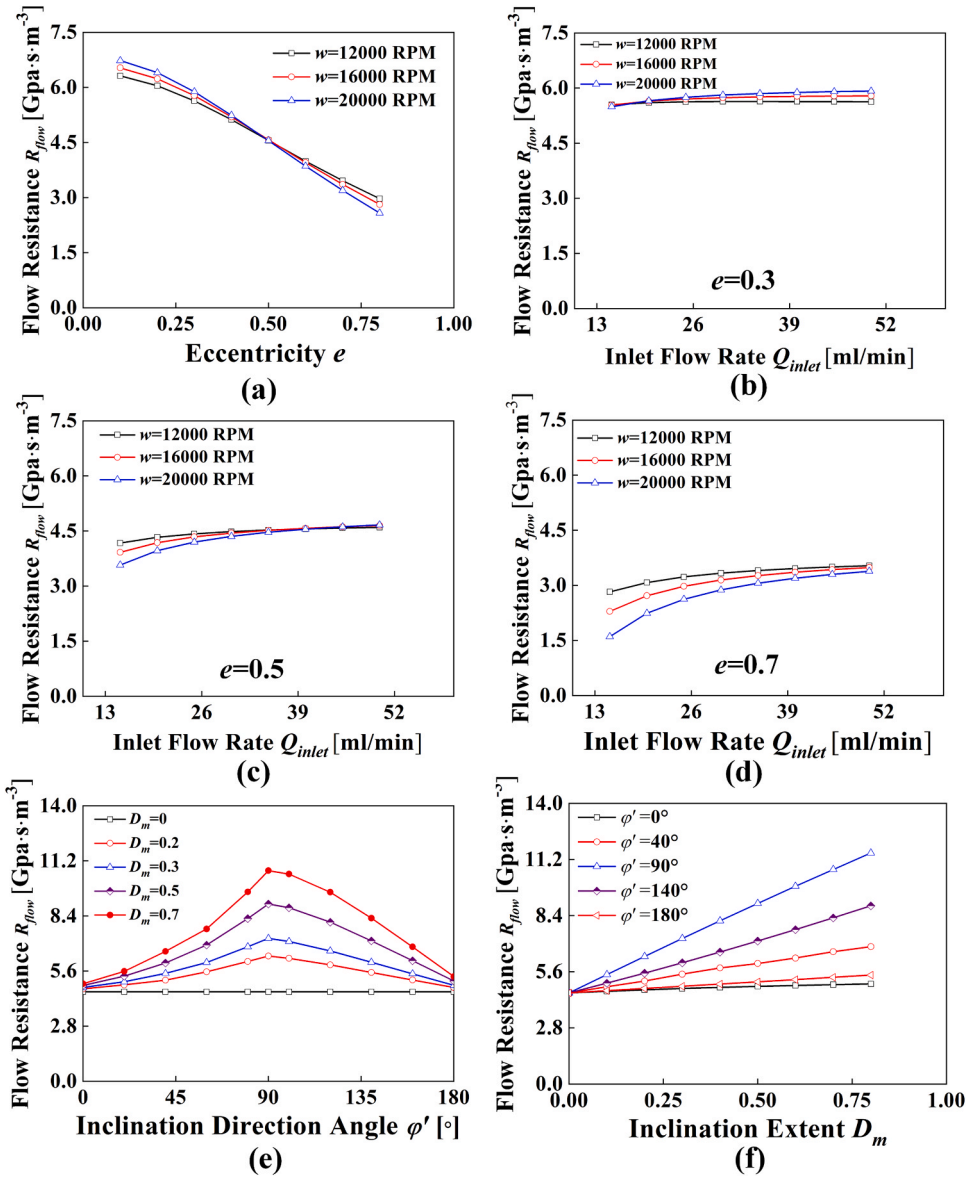

Fig. 11. (a) Flow resistance (R_{flow}) of the journal bearing under different rotating eccentricities from 0.1 to 0.8. R_{flow} plots as a function of inlet flow rate at (b) e= 0.3, (c) e= 0.5 and (d) e= 0.7. The variation in R_{flow} with (e) the inclination angle φ' and (f) inclination extent D_m at e= 0.5, ω = 20000 RPM and Q_{inlet} = 40 ml/min.

Notably, the overall pressure value in the axial bearing is closely related to the boundary value $P_{interface}$, which is determined by Q_{inlet} through the journal bearing. For the journal bearing, the fluid flows from the bottom end to the upper end, and in this process, the fluid must overcome the ambient pressure p_a and the flow resistance R_{flow}. R_{flow} can be defined as:

$$R_{flow} = \frac{P_{\text{int erface}} - P_a}{Q_{inlet}} \tag{53}$$

Thus, given the ambient pressure p_a and flow rate, $P_{interface}$ is inherently determined by R_{flow}. Hence, the dependence of R_{flow} on various operation parameters is quantified.

Fig. 11(a) presents the plots of R_{flow} as a function of the eccentricity for different rotating speeds at Q_{inlet} = 40 ml/min. It is obtained that R_{flow} obviously decreases with increasing e. A threshold of the eccentricity ($e_{critical}$) exists, below which R_{flow} increases with a rotating speed (ω), but the contrary is true when e>$e_{critical}$. Furthermore, the variation in R_{flow} as a function of Q_{inlet} is plotted in Fig. 11(b)-(d) at e= 0.3, 0.5 and 0.7, respectively. The results show that there is a positive correlation between R_{flow} and Q_{inlet}, and the increasing trend becomes slower at lower ω and larger e. Additionally, it can be inferred from Fig. 11(b)-(d) that $e_{critical}$ increases when Q_{inlet} increases. Fig. 11(e)-(f) display the variation in R_{flow} with the inclination angle φ' and inclination extent D_m, respectively. The results show that R_{flow} almost linearly increases with D_m but first increases with φ' when $\varphi' < 90°$ and then decreases with φ' when $\varphi' > 90°$.

4.2. Lubrication performances in different positions

Due to the non-rigid characteristics of JAHBs, the rotor's position changes during operation. The analytical model is utilized to explore the load capacity and the friction feature under different eccentricities and axial clearance (s_2). Fig. 12(a) shows the levitation force variation curves with e at ω = 20000 RPM and Q_{inlet}= 40 ml/min. It can be observed that the radial levitation force (F_r) increases exponentially with an increasing eccentricity, which is consistent with the larger pressure difference shown in Fig. 8(a)-(c). However, the axial levitation force (F_a) decreases with an increasing e. From the analysis above, the flow resistance of the journal bearing (R_{flow}) declines with e, thus resulting in a reduction in $P_{interface}$ based on Eq. (53). Furthermore, as shown in Fig. 8(d)-(f), since the unevenness of the leakage flow is intensified with eccentricity, both the inward flow and the outward flow are enhanced. However, from the analysis presented in Section 4.1, the reduction effect of the inward flow is more obvious than the enhancement effect of the outward flow on the pressure distribution. Thus, both the flow rate change and the $P_{interface}$ reduction brought by an increasing eccentricity led to a decline in F_a. Fig. 12(b) presents the plots of the levitation force as a function of s_2. F_r remains unchanged when s_2 varies. However, the effect of increasing s_2 on enhancing F_a is not obvious and saturates. When s_2 increases from 1 mm to 3 mm, F_a only faintly increases by 0.23 N. From this phenomenon, it can be inferred that the terms appearing with $2R^{\frac{8}{5}}/(S\mathrm{Re}^{1/5})$ in Eq. (35) are quite small and may be eliminated for simplification. Moreover, the centrifugal force term $2RK^2$ dominates the pressure distribution. Since the gravity of the rotor is only 0.14 N, the levitation force is one order of magnitude larger than the gravity in each direction, manifesting the excellent load capacity of the JAHB.

The total friction torque (T_f) distribution of the JAHB and the ratio of the journal bearing friction are presented in Fig. 12(c) and (d), respectively. Due to levitation, the friction torque of the JAHB is dramatically reduced, and T_f is less than 1 mN·m at 20000 RPM, as shown in Fig. 12(c). Furthermore, s_2 has a slight enhancing effect on T_f, and T_f is also aggravated by the eccentricity. Fig. 12(d) illustrates that the journal bearing is the main source of the friction torque, which provides more than 67% of T_f. Additionally, the ratio of the journal bearing friction increases slightly when enlarging the eccentricity and decreasing s_2.

4.3. Lubrication performance under different operating conditions

Regarding the JAHB, the inlet flow rate (Q_{inlet}) and the rotating speed

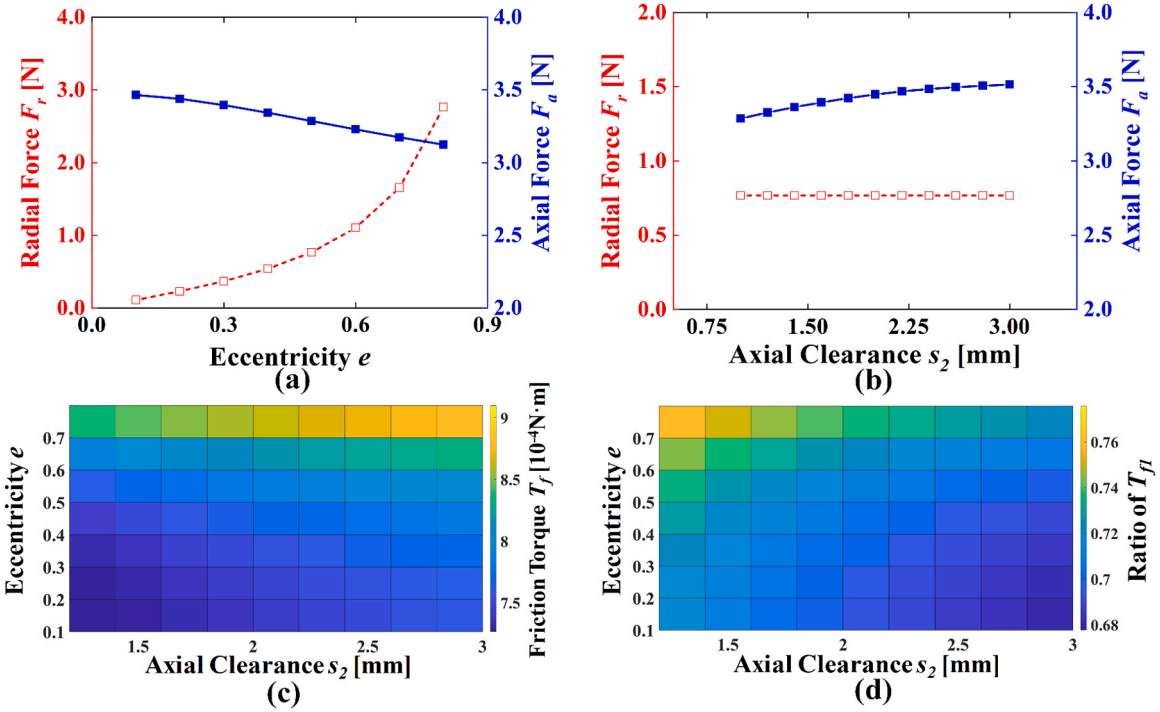

Fig. 12. Levitation force of the JAHB at ω = 20000 RPM and Q_{inlet}= 40 ml/min under (a) different eccentricities and (b) different axial clearances. (c) The friction torque distribution of the JAHB with eccentricity and axial clearance. (d) Distribution of the friction torque ratio of the journal bearing with eccentricity and axial clearance.

(ω) are the primary operational parameters. Here, the relationship between the levitation force and Q_{inlet} is plotted in Fig. 13(a). At e= 0.5 and s_2= 1 mm, the results show that F_a almost linearly increases with Q_{inlet}, which is consistent with the experimental data. Moreover, this increase can be explained by the increase in the boundary pressure ($P_{interface}$) with an increasing Q_{inlet}, according to Eq. (53). Although $P_{interface}$ increases, F_r doesn't change, since the enhancement of the overall pressure is neutralized during the integration of Eqs. (13) and (14). Fig. 13(d) depicts the variation in the levitation force as a function of ω. It is illustrated that when ω increases, a linear correlation holds between F_r, as described by Eq. (1), in which all the pressure terms are linearly coupled with ω. However, F_a decreases significantly with an increasing ω. The mechanism may be attributed to the dominance of the centrifugal force term $2RK^2$ in Eq. (35). This term is proportional to ω^2 based on the dimensional analysis, which leads to a larger pressure gradient from the disc periphery to the disc center.

Additionally, the dependence of the friction torque on Q_{inlet} and ω is displayed in Fig. 13(c) and (d). As expected, T_f dramatically increases when ω rises. Specifically, a 138% increase in T_f is obtained when the rotating speed changes from 12,000 RPM to 22,000 RPM. It seems that the axial friction rises more rapidly with ω since the journal bearing friction accounts for a reduced ratio of T_f at higher ω, as shown in Fig. 13 (d). However, the friction feature of the JAHB shows no obvious relevance to the flow rate, as illustrated in Fig. 13(c) and (d).

4.4. Effect of the inclination on the lubrication performance

During operation, the external force moment and the asymmetric pressure distribution on the end face of the rotor may cause an inclination in the rotor. Fig. 14(a) and (b) show the change in the levitation force with the inclination parameters, including the direction angles φ' and inclination extent D_m when e = 0.5. From Eqs. (9)-(11), the inclination angle α decreases with D_m and reaches a maximum at φ' = 90°. In the case of e = 0.5, the maximum α is 2.32° at D_m = 1 and φ' = 90°, and the resulting extreme deviation of s_2 is 0.51 mm. Because F_a is not sensitive to s_2, the impact of a 0.51 mm change in s_2 on the variation in F_a is less than 3.2% according to the results in Fig. 12(b). Thus, the influence of the inclination on the axial clearance of the axial bearing is neglected. Fig. 14(a) shows that F_a rises to a maximum value at φ'= 90° and then falls with an increasing φ', which is consistent with the tendency between R_{flow} and φ'. F_r is almost unchanged with φ' at small D_m, but at high D_m, F_r fluctuates with φ', and a local maximum point can be observed at φ' = 90°. Generally, the fluctuation of F_r when changing φ' is not obvious, and the extreme deviation of F_r is only 0.117 N when D_m = 0.8. From Fig. 14(b), it can be seen that F_a slightly increases with D_m, which may be related to the linear relation between R_{flow} and D_m, while F_r increases faster with an increasing D_m. The average increase in F_a at various φ' is only 0.27 N when D_m increases from 0 to 0.8. The T_f distribution of the JAHB is shown in Fig. 14(c) and (d). It can be seen that both T_f and the ratio of T_{f1} reach the peak at φ' = 90° and increase with D_m.

5. Conclusions

In this work, a turbulent lubrication model of a novel journal-axial coupled hydrodynamic bearing (JAHB) is developed. In this model, the fluid flow in the journal bearing and that in the axial bearing are bridged to predict the whole pressure field in the JAHB. The momentum transfer behavior on the interface between the journal bearing and the axial bearing is investigated. The results show that the interface flow is asymmetric with the eccentricity of the journal bearing and therefore causes pressure unevenness in the axial bearing. Mechanism analysis reveals that the centrifugal force acting on the fluid dominates the radial pressure distribution of the axial bearing and enlarges the pressure drop from outlet to inlet. The inward flow into the axial bearing accelerates the angular motion of the fluid and therefore weakens the pressure field, while the outward flow enhances it. The proposed model has been validated by the experiment with less than 15% error for the whole range of working conditions. Furthermore, the model is utilized to investigate the lubrication performances under various operating conditions. At the rotating speed of 20000 RPM, the load capacity of JAHB is one order of magnitude larger than the rotor's gravity, while the friction

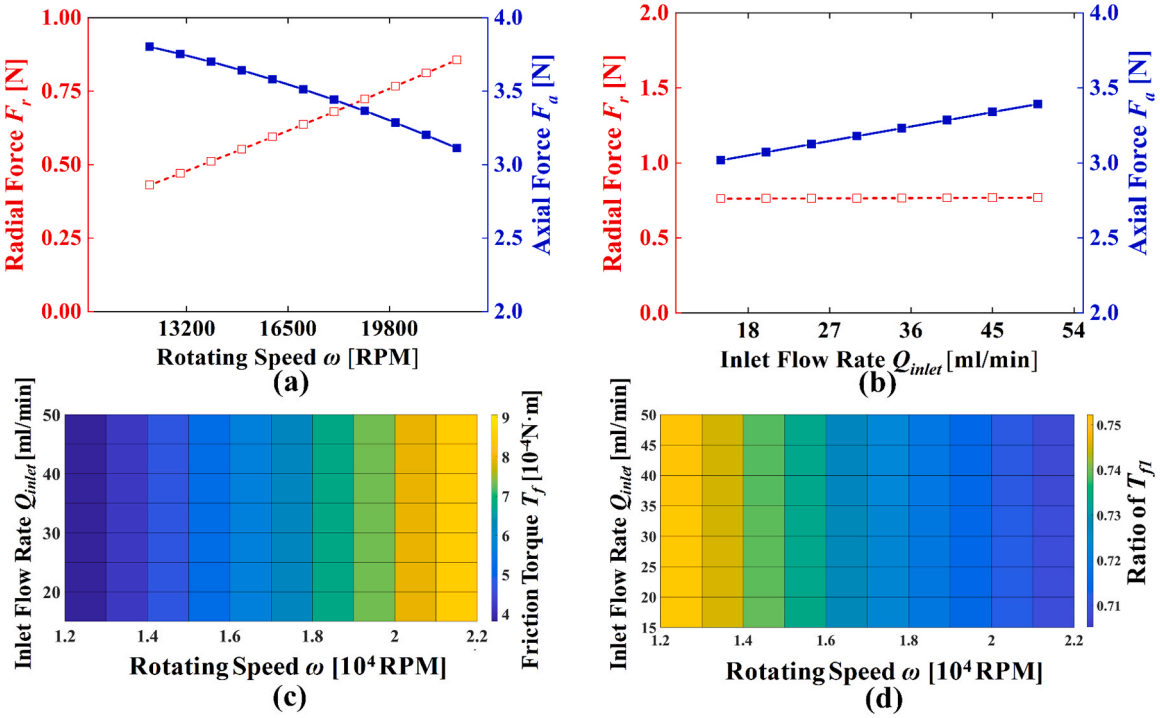

Fig. 13. Levitation force of the JAHB at e= 0.5 and s_2= 1 mm under (a) different rotating speeds and (b) different inlet flow rates. (c) The friction torque distribution of the JAHB with a rotating speed and inlet flow rate. (d) Distribution of the friction torque ratio of the journal bearing with a rotating speed and inlet flow rate.

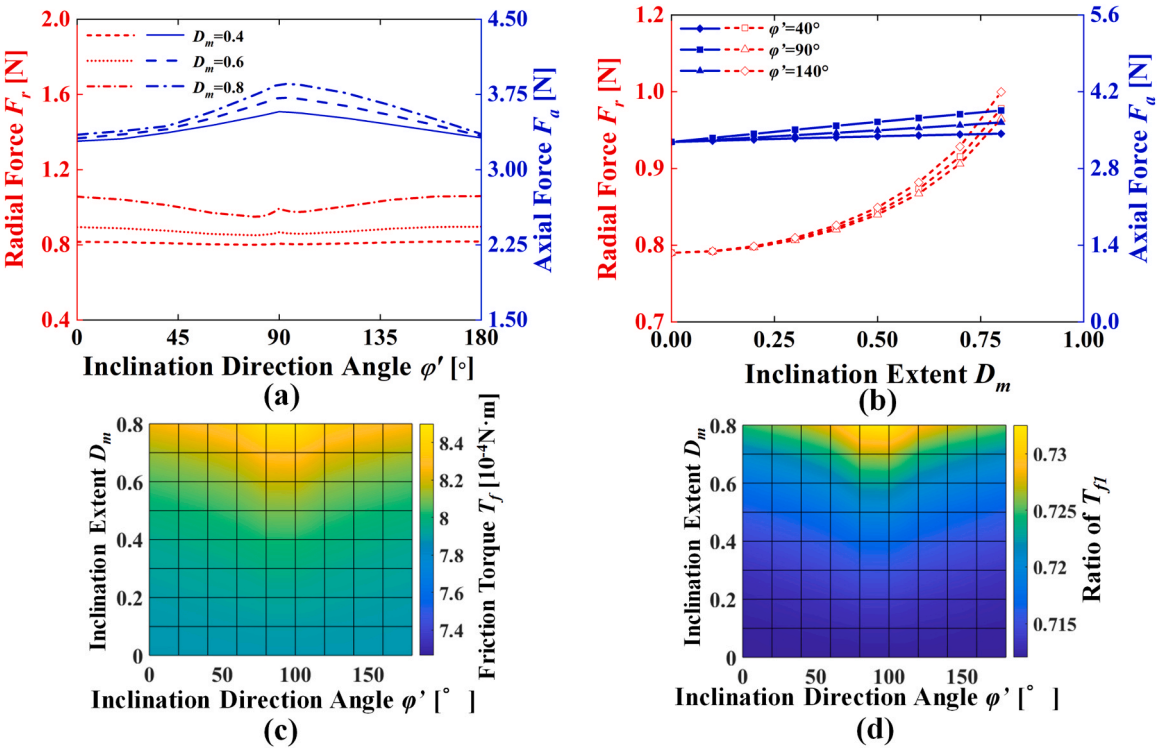

Fig. 14. Levitation force of the JAHB at e= 0.5 and s_2= 1 mm under (a) different inclination direction angles φ' and (b) different inclination extents D_m. (c) The friction torque distribution with φ' and D_m. (d) Distribution of the friction torque ratio of the journal bearing with φ' and D_m.

torque is less than 1 mN·m. Therefore, the JAHB may be a promising option for reliable bearings in high-speed turbomachines.

Declaration of Competing Interest

The authors declare that they have no known competing financial interests or personal relationships that could have appeared to influence the work reported in this paper.

Data availability

No data was used for the research described in the article.

Acknowledgments

The authors would like to acknowledge the financial support from the Fundamental Research Funds for the Central Universities (HUST: 2023JYCXJJ026) and the National Key R & D Project from Ministry of Science and Technology of China (Grant No. 2022YFA1203100).

Appendix A. Supporting information

Supplementary data associated with this article can be found in the online version at doi:10.1016/j.triboint.2023.109036.

References

[1] Duan B, Luo M, Yuan C, Luo X. Multi-objective hydraulic optimization and analysis in a minipump. Sci Bull 2015;60(17):1517–26.
[2] Ren T, Feng M. Anti-shock characteristics of water lubricated bearing for fuel cell vehicle air compressor. Tribol Int 2017;107:56–64.
[3] Merelli CE, Barilá DO, Vignolo GG, Quinzani LM. Dynamic coefficients of finite length journal bearing. Evaluation using a regular perturbation method. Int J Mech Sci 2019;151:251–62.
[4] Agrawal N, Sharma SC. Micro-grooved hybrid spherical thrust bearing with Non-Newtonian lubricant behaviour. Int J Mech Sci 2023;240:107940.
[5] Xiang G, Wang J, Han Y, Yang T, Dai H, Yao B, Zhou C, Wang L. Investigation on the nonlinear dynamic behaviors of water-lubricated bearings considering mixed thermoelastohydrodynamic performances. Mech Syst Signal Process 2022;169:108627.
[6] Yu Y, Pu G, Jiang T, Jiang K. Discontinuous grooves in thrust air bearings designed with CAPSO algorithm. Int J Mech Sci 2020;165:105197.
[7] Luan W, Liu Y, Wang Y, Xu F. Effect of herringbone groove structure parameters on the static performance of gas foil herringbone groove thrust bearings. Tribol Int 2022;177:107979.
[8] Kim K, Lee M, Lee S, Jang G. Optimal design and experimental verification of fluid dynamic bearings with high load capacity applied to an integrated motor propulsor in unmanned underwater vehicles. Tribol Int 2017;114:221–33.
[9] Andres LS. Effect of shaft misalignment on the dynamic force response of annular pressure seals. Tribology Trans 1993;36(2):173–82.
[10] Dai H, Xiang G, Wang J, Guo J, Wang C, Jia H. Study on time-varying mixed lubrication performance of microgroove journal-thrust coupled bearing under water lubrication. Ind Lubr Tribology 2022;74.
[11] Nanbu T, Ren N, Yasuda Y, Zhu D, Wang QJ. Micro-textures in concentrated conformal-contact lubrication: effects of texture bottom shape and surface relative motion. Tribol Lett 2008;29(3):241–52.
[12] Sahu K, Sharma SC, Ram N. Misalignment and Surface Irregularities Effect in MR Fluid Journal Bearing. Int J Mech Sci 2022;221:107196.
[13] Ausas R, Jai M, Buscaglia G. A mass-conserving algorithm for dynamical lubrication problems with cavitation. J Tribology-TRANS ASME - J TRIBOL-TRANS ASME 2009;131.
[14] Sun F, Zhang X, Wei Y, Wang X, Wang D. Stability analysis of rubber-supported thrust bearing in a rotor-bearing system used in marine thrusters under disturbing moments. Tribol Int 2020;151:106356.
[15] Adatepe H, Bıyıklıoglu A, Sofuoglu H. An investigation of tribological behaviors of dynamically loaded non-grooved and micro-grooved journal bearings. Tribol Int 2013;58:12–9.
[16] Ene N, Dimofte F, Keith T. A stability analysis for a hydrodynamic three-wave journal bearing. Tribol Int 2008;41:434–42.
[17] Smolík L, Rendl J, Omasta M, Byrtus M, Šperka P, Polach P, Hartl M, Hajžman M. Comprehensive analysis of fluid-film instability in journal bearings with mechanically indented textures. J Sound Vib 2023;546:117454.
[18] Pattnayak MR, Ganai P, Pandey RK, Dutt JK, Fillon M. An overview and assessment on aerodynamic journal bearings with important findings and scope for explorations. Tribol Int 2022;174:107778.
[19] R. Wu, W. Lan, X. Yu, S. Weicheng, M. Wang, X. Luo, Numerical Study of the Flow Condition of the Hydrodynamic Levitated Mechanical Micropump, 2018.
[20] Jang GH, Kim YJ. Calculation of dynamic coefficients in a hydrodynamic bearing considering five degrees of freedom for a general rotor-bearing system. J Tribol 1999;121(3):499–505.
[21] Peixoto TF, Cavalca KL. Investigation on the angular displacements influence and nonlinear effects on thrust bearing dynamics. Tribol Int 2019;131:554–66.
[22] Luo X., Liu F., Duan B., et al. Micro Hydraulic Suspension Mechanical Pump. US Patent, US 10495093B2, 2019–12-03.

[23] Xing G, Song X, Hong T, Zuo H, Luo X. A novel hydrodynamic suspension micropump using centrifugal pressurization and the wedge effect. Sci China Technol Sci 2023;66.
[24] Zuo H, Xue S, Hong T, Xing G, Han J, Ma J, Hu R, Luo X. Theoretical and experimental analysis of the centrifugal micro hydrodynamic axial-thrust bearing. Tribol Int 2023;187:108696.
[25] Xing G, Hong T, Xue S, Ke H, Luo X. The trajectory monitoring method of hydrodynamic suspension bearing based on laser-ranging technology. Meas Sci Technol 2023;34(8):085008.
[26] Feng H, Jiang S, Ji A. Investigations of the static and dynamic characteristics of water-lubricated hydrodynamic journal bearing considering turbulent, thermohydrodynamic and misaligned effects. Tribol Int 2019;130:245–60.
[27] Ferron J, Frene J, Boncompain R. A study of the thermohydrodynamic performance of a plain journal bearing comparison between theory and experiments. J Lubr Technol 1983;105(3):422–8.
[28] Xiang G, Han Y, Chen R, Wang J, Ni X, Xiao K. A hydrodynamic lubrication model and comparative analysis for coupled microgroove journal-thrust bearings lubricated with water. Proc Inst Mech Eng, Part J: J Eng Tribology 2019;234(11): 1755–70.
[29] Shi J, Zhao B, He T, Tu L, Lu X, Xu H. Tribology and dynamic characteristics of textured journal-thrust coupled bearing considering thermal and pressure coupled effects. Tribol Int 2023;180:108292.
[30] Wang Y, Wang Q, Lin C. A mixed-EHL analysis of effects of misalignment and elastic deformations on the performance of a coupled journal-thrust system. Tribol Int 2006;39:281–9.
[31] Sun J, Changlin G. Hydrodynamic lubrication analysis of journal bearing considering misalignment caused by shaft deformation. Tribol Int 2004;37:841–8.
[32] Xiang G, Wang J, Zhou C, Shi Y, Wang Y, Cai J, Wang C, Jin D, Han Y. A tribo-dynamic model of coupled journal-thrust water-lubricated bearings under propeller disturbance. Tribol Int 2021;160:107008.
[33] Bayley F, Owen J. Flow between a Rotating and a Stationary Disc. Aeronaut Q 1969;20:333–54.
[34] Qiao J, Zhou G, Pu W, Li R, He M. Coupling analysis of turbulent and mixed lubrication of water-lubricated rubber bearings. Tribol Int 2022;172:107644.
[35] Kango S, Sharma RK, Pandey RK. Thermal analysis of microtextured journal bearing using non-Newtonian rheology of lubricant and JFO boundary conditions. Tribol Int 2014;69:19–29.
[36] Elrod Jr HG, Ng CW. A theory for turbulent fluid films and its application to bearings. J Lubr Technol 1967;89(3):346–62.
[37] J. Daily, R. Arndt, Enclosed Rotating Disks with Superposed Throughflow: A Survey of Basic Effects, 1962.
[38] Itoh M, Yamada Y, Imao S, Gonda M. Experiments on turbulent flow due to an enclosed rotating disk. Exp Therm Fluid Sci 1992;5:359–68.
[39] Schlichting H, Gersten K. Boundary-Layer Theory. Berlin, Heidelber: Springer Berlin Heidelberg,; 2017.
[40] I. Shevchuk, Convective Heat and Mass Transfer in Rotating Disk Systems, 2009.
[41] von Kármán T. On the statistical theory of turbulence. Proc Natl Acad Sci 1937;23 (2):98–105.